Inelastic light scattering spectroscopy in si/SiGe nanostructures: strain, chemical composition and thermal properties

Tsybeskov, L.; Mala, S. A.; Wang, X.; Baribeau, J.-M.; Wu, X.; Lockwood, D. J.

Publisher's version / Version de l'éditeur:
https://doi.org/10.1016/j.ssc.2016.07.008
Solid State Communications, 2016-07-09

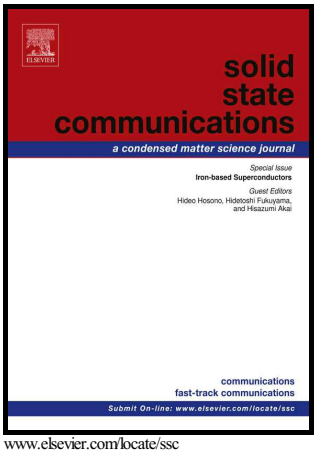

www.elsevier.com/locate/ssc

Inelastic light scattering spectroscopy in si/SiGe nanostructures: Strain, chemical composition and thermal properties

L. Tsybeskov, S.A. Mala, X. Wang, J.-M. Baribeau, X. Wu, D.J. Lockwood

PII: S0038-1098(16)30154-5
DOI: http://dx.doi.org/10.1016/j.ssc.2016.07.008
Reference: SSC12984

To appear in: *Solid State Communications*

Received date: 8 June 2016
Accepted date: 8 July 2016

Cite this article as: L. Tsybeskov, S.A. Mala, X. Wang, J.-M. Baribeau, X. Wu and D.J. Lockwood, Inelastic light scattering spectroscopy in si/SiG nanostructures: Strain, chemical composition and thermal properties, *Solid Stat Communications,* http://dx.doi.org/10.1016/j.ssc.2016.07.008

Inelastic Light Scattering Spectroscopy in Si/SiGe Nanostructures: Strain, Chemical Composition and Thermal Properties

L. Tsybeskov[1*], S. A. Mala[1], X. Wang[1], J.-M. Baribeau[2], X. Wu[2] and D. J. Lockwood[2]

[1] Department of Electrical and Computer Engineering, New Jersey Institute of Technology, Newark, NJ 07102, USA

[2] National Research Council, Ottawa, ON KIA 0R6, Canada

Abstract

We present a review of recent studies of inelastic light scattering spectroscopy in two types of Si/SiGe nanostructures: planar superlattices and cluster (dot) multilayers including first- and second-order Raman scattering, polarized Raman scattering and low-frequency inelastic light scattering associated with folded acoustic phonons. The results are used in semi-quantitative analysis of chemical composition, strain and thermal conductivity in these technologically important materials for electronic and optoelectronic devices.

Keywords: A. Nanostructures; B. Molecular Beam Epitaxy; D. Inelastic Light Scattering; E. Raman Scattering

*Corresponding author: leonid.tsybeskov@njit.edu

1. Introduction

Inelastic light scattering is an important characterization technique providing a great deal of information about the structural and electronic properties of Si/SiGe nanostructures [1-5]. A light scattering event in semiconductor nanostructures involves a variety of phonons and produce additional spectral peaks with wavenumbers between bulk acoustic phonons and optical phonons [6]. In Si/SiGe nanostructures, similar to bulk SiGe alloys, the Raman spectrum is

composed of three major bands with a Si-like (Si) peak at ~ 500 cm^{-1}, an alloy-like (SiGe) peak at ~ 400 cm^{-1}, a Ge-like (Ge) peak at ~ 300 cm^{-1}, and weaker Raman features located between the three major peaks [1-5, 7, 8]. These weaker Raman features are attributed to local vibration modes (*e.g.,* Si-Si in the presence of a Ge atom, etc.) and various overtones [6, 9]. Light scattering at low wavenumbers (< 100 cm^{-1}) is related to processes associated with various acoustic phonons, and second-order Raman scattering produces multiple overlapping peaks located between 600 and 1200 cm^{-1} [6]. Thus, in Si/SiGe nanostructures the entire spectral region of 0-1200 cm^{-1} is covered by multiple Raman peaks, and these peaks exhibit strong dependence on growth conditions, strain, temperature and chemical composition.

The intensity of the Raman signal is proportional to the Raman cross-section and the scattering volume, which is related to the light penetration depth and hence the optical absorption coefficient. Resonant Raman scattering (RRS) is associated with significant changes in the Raman cross section, which are directly related to the joint density of states in the electronic bands of bulk materials or nanostructures. While crystalline Si (c-Si) does not exhibit any resonances within the entire visible spectrum, c-Ge has a well-known resonance around 2.2 eV associated with E_1 and $E_1 + \Delta_1$ electronic transitions in the L direction of the Brillouin zone [6]. Thus, in Si/SiGe nanostructures the Raman signal intensity as a function of the excitation light photon energy exhibits a broad peak around 2.2– 2.5 eV [10-11]. The optical polarization dependence of the Raman scattering intensity is defined by the Raman tensors [6]. In Si/SiGe nanostructures, this technique has been successfully used to detect various imperfections in epitaxially grown samples, including inhomogeneous strain [12-14].

This review is intended to cover the following topics:

1. Inelastic light scattering in various Si/SiGe nanostructures including processes associated with acoustic and optical phonons.

2. Analysis of strain and composition in Si/SiGe nanostructures using light-scattering spectroscopy.

3. Evaluation of Si/SiGe nanostructure thermal properties using Raman scattering.

4. Application of polarized Raman scattering in detecting strain in Si/SiGe nanostructures.

2. Growth and structural properties of Si/SiGe nanostructures: Superlattices and cluster multilayers.

Si/SiGe superlattices (SLs) are formed using alternating thin layers of Si and $Si_{1-x}Ge_x$ with $x<0.5$ grown by molecular beam epitaxy (MBE) on (001) Si substrates at a temperature of ~ 500^{o}C (see Fig. 1a and ref. 15). This relatively low growth temperature is chosen to realize dislocation-free pseudomorphic growth, prevent Si/SiGe intermixing, and reduce the interface roughness. For a SiGe layer with thickness below a critical value, the lattice mismatch between Si and SiGe is anticipated to be accommodated by a homogeneous tetragonal compression. These compressed SiGe layers are combined with alternating, in most cases strained, Si layers and form $Si/Si_{1-x}Ge_x/Si$ strained-layered SLs.

Si/SiGe cluster multilayers (CM) (Fig. 1b) are grown using SiGe thicknesses approaching or above critical values, and the growth of SiGe on Si requires relief of the elastic energy in the strained SiGe film [16]. At high growth temperature, the adatom diffusion and elastic deformation trigger a transition from two-dimensional to three-dimensional growth modes. This growth mechanism is known as Stranki-Krastanov (S-K) growth, and it is performed at 550-650^{o}C. In chemical vapor deposition based S-K growth, GeH_4 diluted in H_2 is used and spontaneous intermixing occurs due to thermal and strain-induced diffusion. In this growth mode, most of the SiGe clusters (or islands) have a pyramid/dome-like (uncapped) or pancake-like (Si capped) shapes with the Ge concentration gradually increasing toward the cluster core [17, 18].

3. First order and low-wavenumber Raman scattering in Si/SiGe nanostructures

Figure 2 shows the Raman spectrum of a $Si/Si_{1-x}Ge_x$ SL (see TEM image on Fig. 1) with the three distinct Raman peaks associated with the Si-Si, Si-Ge and Ge-Ge local bond vibrations. In addition to the major Si-Si Raman peak at 520 cm^{-1} with FWHM of 5-6 cm^{-1}, a weaker peak at 505-506 cm^{-1} attributed to strained Si is found [5, 9, 15]. In both Si/SiGe SLs and S-K CMs, curve fitting indicates that the FWHM of the 505-506 cm^{-1} peak precisely correlates with the

FWHM of the major Raman peak at 520 cm^{-1} [9]. It was concluded that in both Si/SiGe SLs and S-K CMs, the Si layers separating SiGe layers are strained and the strain in SL Si layers is more homogeneous compared to that found in CMs [9]. $Si/Si_{1-x}Ge_x$ nanostructures with $x \geq 0.4$ and thicker SiGe layers usually show the main Raman peak at ~ 490 cm^{-1} (Fig. 3) instead of at 520 cm^{-1}, which is attributed to the local Si-Si vibration mode in the presence of Ge [7]. However, if the excitation wavelength is long enough to reach the c–Si substrate, Raman peaks at 520, 508 and 490 cm^{-1} can be observed (Fig. 3).

Raman spectra associated with Si-Ge and Ge-Ge vibrations are peaked at 417-418 cm^{-1} and 298-299 cm^{-1}, respectively (Fig. 4). In S-K CM samples, the Si-Ge and Ge-Ge peaks are broader by ~3 cm^{-1} and are slightly shifted toward lower wavenumbers compared to that in SL samples. In addition, the Raman spectra show weaker and broader peaks at ~250 cm^{-1} attributed to the resonant Ge vibrational mode and at 438 cm^{-1} associated with the local Si vibrational mode in the presence of Si and Ge, respectively [19, 20] These peaks are enhanced in S-K CMs compared to SL samples, most likely due to the higher Ge composition. Figure 5a presents a summary of the reported dependence of the Raman peak wavenumbers associated with Si-Si, Si-Ge and Ge-Ge vibrations on the composition x in bulk $Si_{1-x}Ge_x$ alloys where there should be no strain [19]. The results are compared to that in Si/SiGe nanostructures with various degree of strain (Fig. 5b), and the following composition dependencies are found:

(a) In bulk $Si_{1-x}Ge_x$ alloys, the Si–Si Raman peak wavenumber linearly decreases with increasing x, as $\omega_{Si-Si} \approx 520 - 70x$. In $Si/Si_{1-x}Ge_x$ nanostructures, the dependence is much weaker $\omega_{Si-Si} \approx 520 - 30x$.

(b) In bulk $Si_{1-x}Ge_x$ alloys, the Ge–Ge Raman peak wavenumber linearly increases with increasing x, $\omega_{Ge-Ge} \approx 280 + 20x$. In $Si/Si_{1-x}Ge_x$ nanostructures, the dependence is stronger; $\omega_{Ge-Ge} \approx 280 + 35x$.

(c) In bulk $Si_{1-x}Ge_x$ alloys, the Si–Ge Raman peak wavenumber increases for $x < 0.6$ and decreases for $x > 0.6$. However, in $Si/Si_{1-x}Ge_x$ nanostructures the dependence can be described as $\omega_{Si-Ge} \approx 400 + 30x$.

The results presented here indicate that apart from average composition x of $Si/Si_{1-x}Ge_x$ nanostructures other factors such as layer thicknesses, SiGe island sizes, shapes and local strain should be to be taken into account in analyzing the dependencies of the Raman peaks. The most common explanation is that an accumulation of Ge in the middle of planar layers and within the SiGe island core is responsible for a non-uniform composition and strain distribution. Possible detailed mechanisms are: the out diffusion of Ge and formation of compressed Si rich alloy regions in the valleys of the $Si_{1-x}Ge_x$ island multilayers, strong diffusion coefficient dependence on the local Ge concentration in the film, and the tensile strain in the Si spacer layer on the top of the SiGe islands [19, 20].

In Si/SiGe periodic nanostructures, multiple Raman peaks at the low wavenumbers (< 100 cm^{-1}) are associated with folding of longitudinal acoustic (FLA) phonons due to the growth introduced new periodicity P_{SL} and formation of the Brillouin mini-zone. A commonly used method for the calculation of phonon dispersion curves is to use the elastic continuum model by Rytov [21]. One of the conditions of this model is that the wavelength of the sound wave should be much larger than the layer thickness. The elastic continuum approximation is then valid and the wave equation in each layer can be solved. Figure 6a shows the low-frequency Raman spectrum in a Si/SiGe SL (shown in Fig. 1a) with distinct Raman doublets corresponding to various FLA modes. The inset shows a simplified FLA phonon dispersion diagram based on Rytov's model. In reality, band gaps appear at the mini-zone center and boundary (Fig. 6b) due to the difference in the acoustic impedances of the two component layers of the SL [22]. These gaps are barriers to phonon propagation along the SL growth direction and having the appropriate energies and wave vectors. Thus, these Si/SiGe periodic nanostructures are the first known examples of one-dimensional phononic crystals [15].

4. Second order Raman scattering in Si/SiGe nanostructures

In Si/SiGe nanostructures, Raman peaks associated with second-order light scattering are observed between 550 and 1100 cm^{-1} (Fig. 11). The two-transverse optical (2TO) Si phonon overtone features are related to scattering from the Brillouin zone critical points at W and L, and they are found at 940 and 975 cm^{-1}, respectively [23, 24]. The 2TO Raman signal is actually

comprised of three peaks: the major Raman peak associated with scattering from 2TO(L) phonons, the 2TO(W) Raman peak, and a weak shoulder associated with the 2TO(Γ) phonon. In most of the Si/SiGe nanostructures we investigated, we also found strong Raman features associated with second order Si-Ge vibrations around 800 cm^{-1} and second order Ge-Ge vibrations at ~ 600 cm^{-1}. Also, other weaker Raman features at ~680 cm^{-1} and in the range of 840-900 cm^{-1} are, most likely, overtones of the first-order Ge-Ge (in the presence of Si) and local Si-Si (in the presence of Ge) modes [24].

5. Strain and chemical composition in $Si/Si_{1-x}Ge_x$ nanostructures

In $Si/Si_{1-x}Ge_x$ nanostructures, a correlation between Si-Si, Si-Ge and Ge-Ge Raman peak positions, Ge content x and strain ε has been extensively discussed [19, 20, 25]. The relative number of chemical bonds comprising the Si-Si, Si-Ge, and Ge-Ge phonon modes are estimated as $(1-x)^2$, $2x(1-x)$, and x^2, respectively. Since the Raman signal is proportional to the scattered volume, the ratio of the integrated Raman peak intensities related to the relative number of chemical bonds of the corresponding phonon modes can be described as follows:

$$I_{GeGe}/I_{SiGe} = Bx/2(1-x), \quad (1)$$

$$I_{SiSi}/I_{SiGe} = A(1-x)/2x, \quad (2)$$

where coefficients A and B are related to the frequencies of the optical modes in the SiGe alloy. It was found experimentally that $B = 3.2$ and $A = 1.85$ for 458 nm excitation [26]. The so-called intensity method for determining the value of x is independent of strain in the alloy layer and depends on the integrated intensity of the Raman signal associated with the phonon bands. In the Raman peak position (the wavenumber method), a set of equations is used, where the peak position of the three major vibrational modes in $Si/Si_{1-x}Ge_x$ nanostructures is described as a function of x and ε. The frequency of the phonon band can be expressed as:

$$\omega = \omega_0 + b\varepsilon, \quad (3)$$

where ω_0 is the x dependent phonon frequency of the unstrained SiGe alloy and b is the strain-shift coefficient. In the case of a strained $Si_{1-x}Ge_x$ ($0<x<0.5$) layer, the wavenumbers of the three

different phonon modes, according to Refs. [25, 26], are:

$$\omega_{Si-Si} = 520.2 - 70.5x - 830\varepsilon, \quad (4)$$

$$\omega_{Si-Ge} = 400.5 + 16.3x - 575\varepsilon, \quad (5)$$

$$\omega_{Ge-Ge} = 282.5 + 16x - 384\varepsilon. \quad (6)$$

The average values of x and ε in the alloy layer are

$$x = \frac{(\omega_{Si-Ge}-400)-(0.7\times(\omega_{Si-Si}-520))}{65}, \quad (7)$$

and

$$\varepsilon = \frac{(400-\omega_{Si-Ge})+0.23\times(520-\omega_{Si-Si})}{767}. \quad (8)$$

Considering published data [9, 19, 20], we find a reasonably good agreement between both methods.

6. Raman studies of thermal conductivity and heat dissipation in $Si/Si_{1-x}Ge_x$ nanostructures

Typically, Raman scattering measurements are performed using an intense laser radiation. While c-Si and c-Ge have high thermal conductivity $k \approx 100$ Wm^{-1} K^{-1}, in compositionally disordered SiGe alloys and Si/SiGe nanostructures $k \leq 10$ W m^{-1} K^{-1} [27]. Thus, a significant temperature increase of a sample might occur during Raman scattering measurements and it will affect the Raman peak position, width and line shape. Using a model based on the Fourier law of heat conduction, the thermal conductivity can be calculated as

$$\kappa = P*(L/A)*(1/\Delta T), \quad (9)$$

where P is the laser power absorbed by a sample with a thickness L in the direction normal to a surface of a cross-sectional area A due to a temperature gradient ΔT. The temperature gradient is established between the highest temperature at the sample surface and the lowest temperature of the c-Si substrate (due to the high c-Si thermal conductivity), and these temperatures can be calculated using the Stokes/anti-Stokes Raman peak intensity ratio for strained Si and Si-Ge

phonon modes and the Si-Si mode at 520 cm^{-1} (assuming that it is associated with the c-Si substrate). In measured samples, the calculated thermal conductivity is ~ 12 W cm^{-1} K^{-1} for Si/Si/SiGe SLs and is ~ 4 W cm^{-1} K^{-1} in Si/SiGe CMs respectively. The reason for the lower thermal conductivity found in Si/SiGe CMs compared to Si/SiGe SLs can be explained by analyzing a comparative volume fraction of SiGe (a lower thermal conductivity material) versus c-Si (a higher thermal conductivity material) and quality of the Si/SiGe heterointerfaces. We find that typically in Si/SiGe CMs, the volume fraction of SiGe is nearly twice that of Si/SiGe SLs, and inelastic scattering of phonons in Si/SiGe nanostructures with a diffuse interface also contributes to the reduction in thermal conductivity [28]. It was also reported that the temperature calculated according to Boltzmann statistics under a non-resonant condition of the Ge-Ge phonon mode is consistently lower than that found for the Si-Ge and Si-Si modes [27]. This discrepancy can be explained assuming that for the used laser excitation wavelengths, the Ge-Ge phonon mode has a resonant component, as it was pointed out in Refs. 9, 29, 30.

7. Polarization dependent Raman scattering in Si/SiGe nanostructures

Polarized Raman scattering provides information on the Raman scattering intensity as a function of the polarization angle of the scattered light [12-14]. The particular shape of the polar plot depends on the symmetry of the vibrational mode being measured and the crystallographic orientation of the sample. Figure 8 shows angular Raman polarization diagrams for three different vibrational modes (Si–Si at 520 cm^{-1}, Si–Ge at 415 cm^{-1}, and Ge–Ge at 298 cm^{-1}) for Si/SiGe S-K CM samples [12]. The observed angular dependencies of the Ge–Ge and Si–Ge Raman mode intensities are nearly identical to that measured in a (100) Si single crystal (solid line). However, a quite different behavior is observed in the Raman polarization dependence for the Si-Si Raman mode at 520. The observed deviation is explained by strain-induced partial relaxation of selection rules, mixing of different phonon modes in the nanometer-thick Si layers separating the SiGe cluster layers and, possibly, in a thin layer of the c-Si substrate directly under the sample. The strong localization of strain observed in the Si layers is consistent with the understanding of the nature of vertical self-ordering produced by strain propagation in Si/SiGe S-K CM nanostructures. Similar measurements performed in Si/SiGe SL samples did not reveal any deviation from the data obtained in (100) c-Si substrates.

Conclusion

In conclusion, this review of the various phenomena associated with first- and second-order inelastic light scattering in Si/SiGe SLs and S-K CMs provides an analysis of the Raman spectrum dependence on strain and chemical composition, discusses low-wavenumber Raman scattering associated with folded acoustic phonon modes in periodic Si/SiGe nanostructures and analyzes a laser-induced sample temperature increase during Raman scattering measurements. The results presented here are important for the development of practical quantitative and non-destructive metrological procedures for a wide variety of SiGe based nanoscale electronic, photonic, and thermoelectric devices. At the same time, we do not discuss in this work several specific techniques such as surface- and tip-enhanced Raman scattering [31] and non-linear Raman scattering [32-33]. We think that these important phenomena require detailed consideration and should be covered in a separate review.

Acknowledgements

We thank our many co-workers and colleagues who have contributed over the last three decades to the Raman studies of SiGe nanostructures, and in particular H.J. Labbé, X. Wu, S. Moisa, and J.P. McCaffrey of the National Research Council, and H.K. Shin. L. Tsybeskov would like to acknowledge support by the Foundation at NJIT, Intel, Hewlett-Packard Laboratories and NSF Award 1027770.

Figure Captions

Figure 1. Cross-sectional transmission electron micrograph (TEM) images of (a) an MBE grown planar $Si/Si_{0.65}Ge_{0.35}$ superlattice and (b) a Si/SiGe cluster multilayer nanostructures.

Figure 2. Raman spectrum of a $Si/Si_{1-x}Ge_x$ superlattice (see TEM image on Fig. 1) showing peaks associated with Si first-order central zone optical phonons (520 cm^{-1}), strained Si (~ 505 cm^{-1}), Si-Ge (~ 400 cm^{-1}) and Ge-Ge (~ 300 cm^{-1}). Raman spectrum of c-Si is shown for comparison. Note logarithmic vertical scale.

Figure 3. Raman spectrum in a $Si/Si_{1-x}Ge_x$ cluster multilayer cluster multilayer nanostructure with $x \approx 0.5$ with the Raman peak at ~ 490 cm^{-1} attributed to the local Si-Si vibration mode in the presence of Ge, or Si-Si measured using 458 nm and 514 nm excitation wavelengths. Note vertical logarithmic scale and Raman peaks at 520, 508 and 490 cm^{-1} under 514 nm excitation.

Figure 4. Raman spectra associated with Si-Ge and Ge-Ge vibrations at 417-418 cm^{-1} and 298-299 cm^{-1} in Si/SiGe Stranski-Krastanov cluster multilayers (S-K CM) and planar superlattices (SL).

Figure 5. A summary of the reported dependencies of the Raman peak wavenumbers associated with Si-Si, Si-Ge and Ge-Ge vibrations on the composition x in (a) bulk $Si_{1-x}Ge_x$ alloys and (b) SiGe nanostructures with various degree of strain. For details, see Ref. 19.

Figure 6. (a) Raman spectra at the low wavenumbers in $Si/Si_{0.65}Ge_{0.35}$ superlattices. The acoustic phonon peaks appear in pairs in accordance with their zone folding index m. The inset shows a schematic of the formation of the Brillouin mini-zone and the anticipated peak positions due to Raman interactions with folded longitudinal acoustic (FLA) phonons for this sample; (b) The measured points and dispersion relation (dashed lines) of the FLA phonons near the mini-zone-edge band gap arising from the difference in the acoustic impedances of the two component layers of the $Si/Si_{0.5}Ge_{0.5}$ SL. For further details, see Ref. [15].

Figure 7. Details of the second order Raman scattering in c-Si and a Si/SiGe suprlattice involving optical phonons at 550-1150 cm^{-1}.

Figure 8. Angular Raman polarization diagrams for Si–Si, Si–Ge, and Ge–Ge vibrational modes for a Si/SiGe Stranski-Krastanov cluster multilayers sample measured using 458 nm laser excitation. A (100) Si single crystal measured Raman polarization diagram is shown for comparison.

References

1. F. Cerdeira, A. Pinczuk, J. C. Bean, B. Batlogg, and B. A. Wilson, Appl. Phys. Lett. 45 (1984) 1138.
2. J. L. Liu, Y. S. Tang, K. L. Wang, T. Radetic, and R. Gronsky, Appl. Phys. Lett. 74 (1999) 1863.
3. E. G. Barbagiovanni, D. J. Lockwood, P. J. Simpson, L. V. Goncharova, J. Appl. Phys. 111 (2012) 034307.
4. J. Menéndez, A. Pinczuk, J. Bevk, J. P. Mannaerts, Journ. Vac. Sc. Techn. B 6 (1988) 1306.
5. B. V. Kamenev, L. Tsybeskov, J.-M. Baribeau, D. J. Lockwood, Appl. Phys. Lett. 84 (2004) 1293.
6. M. Cardona, Y. Y. Peter, Fundamentals of semiconductors. Springer-Verlag Berlin Heidelberg (2005) 619.
7. M. I. Alonso, K. Winer, Physical Review B 39 (1989) 10056.
8. P. M. Mooney, F. H. Dacol, J. C. Tsang, J. O. Chu, Appl. Phys. Lett. 62 (1993) 2069.
9. S. A. Mala, L. Tsybeskov, D. J. Lockwood, X. Wu, X., and J. M. Baribeau, J. Appl. Phys., 116, (2014) 014305.
10. F. Cerdeira, M. I. Alonso, D. Niles, M. Garriga, M. Cardona, E. Kasper, H. Kibbel, Phys. Rev. B 40 (1989) 1361.
11. M. Cazayous, J. R. Huntzinger, J. Groenen, A. Mlayah, S. Christiansen, H. P. Strunk, O. G. Schmidt, and K. Eberl, Phys. Rev. B 62 (2000) 7243.
12. B. V. Kamenev, H. Grebel, L. Tsybeskov, T. I. Kamins, R. S. Williams, J.-M. Baribeau, D. J. L. Lockwood. Appl. Phys. Lett. 83 (2003) 5035.
13. M. Mermoux, A. Crisci, F. Baillet, V. Destefanis, D. Rouchon, A. M. Papon, J. M. Hartmann, J. Appl. Phys. 107 (2010) 013512.
14. A. V. Baranov, A. V. Fedorov, T. S. Perova, R. A. Moore, V. Yam, D. Bouchier, V. Le Thanh, K. Berwick, Phys. Rev. B 73 (2006) 075322.
15. D. Zhang, D. J. Lockwood, H. J. Labbé, and J.-M. Baribeau. Phys. Rev. B 46 (1992) 9881.
16. D. J. Eaglesham, M. Cerullo, Phys. Rev. Lett. 64 (1990) 1943.

17. F. M. Ross, J. Tersoff, R. M. Tromp. Phys. Rev. Lett. 80 (1998) 984.
18. J. A. Floro, E. Chason, L. B. Freund, R. D. Twesten, R. Q. Hwang, and G. A. Lucadamo. Phys. Rev. B 59 (1999) 1990.
19. H. K. Shin, D. J. Lockwood, and J. M. Baribeau, Solid State Commun., 114, (2000) 505.
20. D. J. Lockwood and J.-M. Baribeau, "Characterization of Strain and Epitaxial Quality in Si/Ge Heterostructures," in *Light Scattering from Semiconductor Structures and Superlattices* (D.J. Lockwood and J.F. Young, Eds.), Plenum, New York, (1991) 197.
21. S. M. Rytov, Sov. Phys. Acoust. 2 (1956) 68.
22. D. Zhang, D. J. Lockwood, H. J. Labbé, and J.-M. Baribeau. Phys. Rev. B 46 (1992) 9881.
23. P. A. Temple and C. E. Hathaway, Phys. Rev. B 7 (1973) 3685.
24. J. S. Lannin, Phys. Rev. B 16 (1977) 1510.
25. T. S. Perova, J. Wasyluk, K. Lyutovich, E. Kasper, M. Oehme, K. Rode, and A. Waldron, J. Appl. Phys. 109 (2011) 033502.
26. P. M. Mooney, F. H. Dacol, J. C. Tsang, and J. O. Chu, Appl. Phys. Lett. 62 (1993) 2069.
27. H.-Y. Chang and L. Tsybeskov, in Silicon Nanocrystals: Fundamentals Synthesis and applications, ed. L. Pavesi, R. Turan, Wiley-VCH, Weinheim, 2010, p. 105.
28. G. Chen, Phys. Rev. B 57 (1998) 14958.
29. K. Brunner, Reports on Progress in Physics 65 (2001) 27.
30. R. Schorer, G. Abstreiter, H. Kibbel, H. Presting, C. Tserbak, and G. Theodorou, Solid State Comm. 93, (1995) 1025.
31. Y. Saito, M. Motohashi, N. Hayazawa, M. Iyoki, and S. Kawata, S. (2006). Appl. Phys. Lett. 88 (2006) 143109.
32. R. Claps, V. Raghunathan, D. Dimitropoulos, and B. Jalali, B. (2004). Opt. Expr. 12 (2004) 2774.
33. H. Rong, A. Liu, R. Jones, O. Cohen, D. Hak, R. Nicolaescu, A. Fang, and M. Paniccia, *Nature* 433 (2005) 292.

Highlights

- Inelastic light scattering in Si/SiGe superlattices and multilayers including processes associated with acoustic and optical phonons is reviewed.
- Raman spectroscopy analysis of strain and chemical composition in Si/SiGe superlattices and multilayers is presented.
- Si/SiGe superlattice and multilayer thermal properties are studied using Raman scattering.
- Polarized Raman scattering is used in detecting strain in Si/SiGe superlattices and multilayers.

Figure

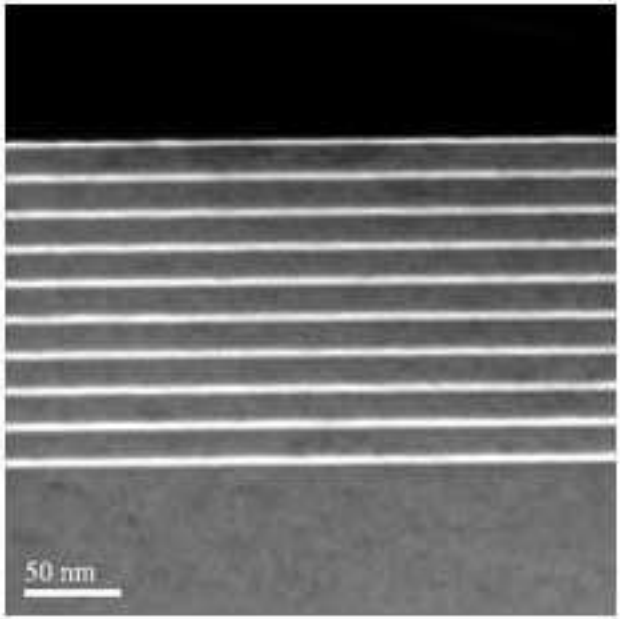

(a)

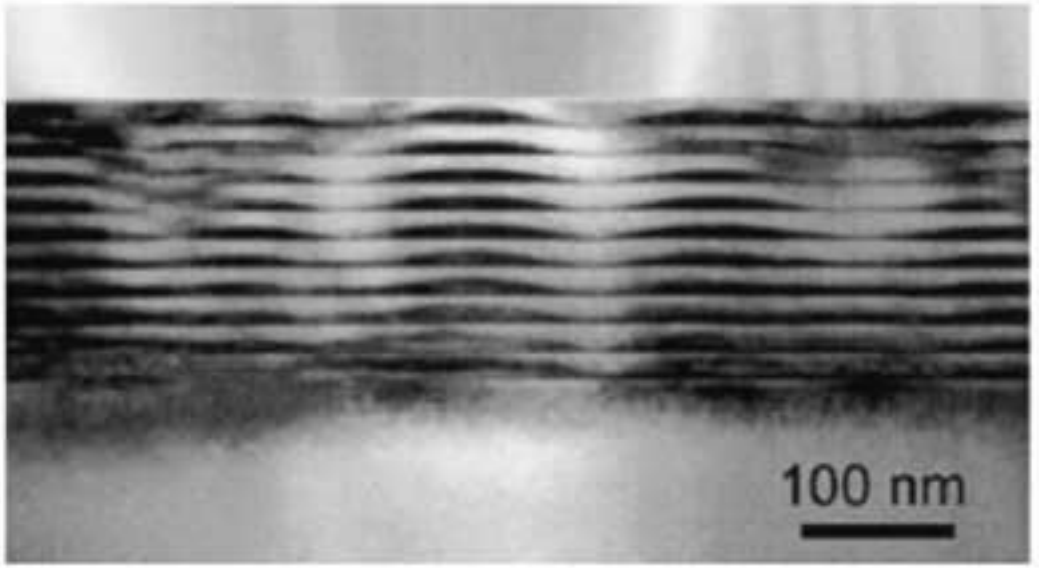

(b)

Tsybeskov et al., Fig. 1

Figure

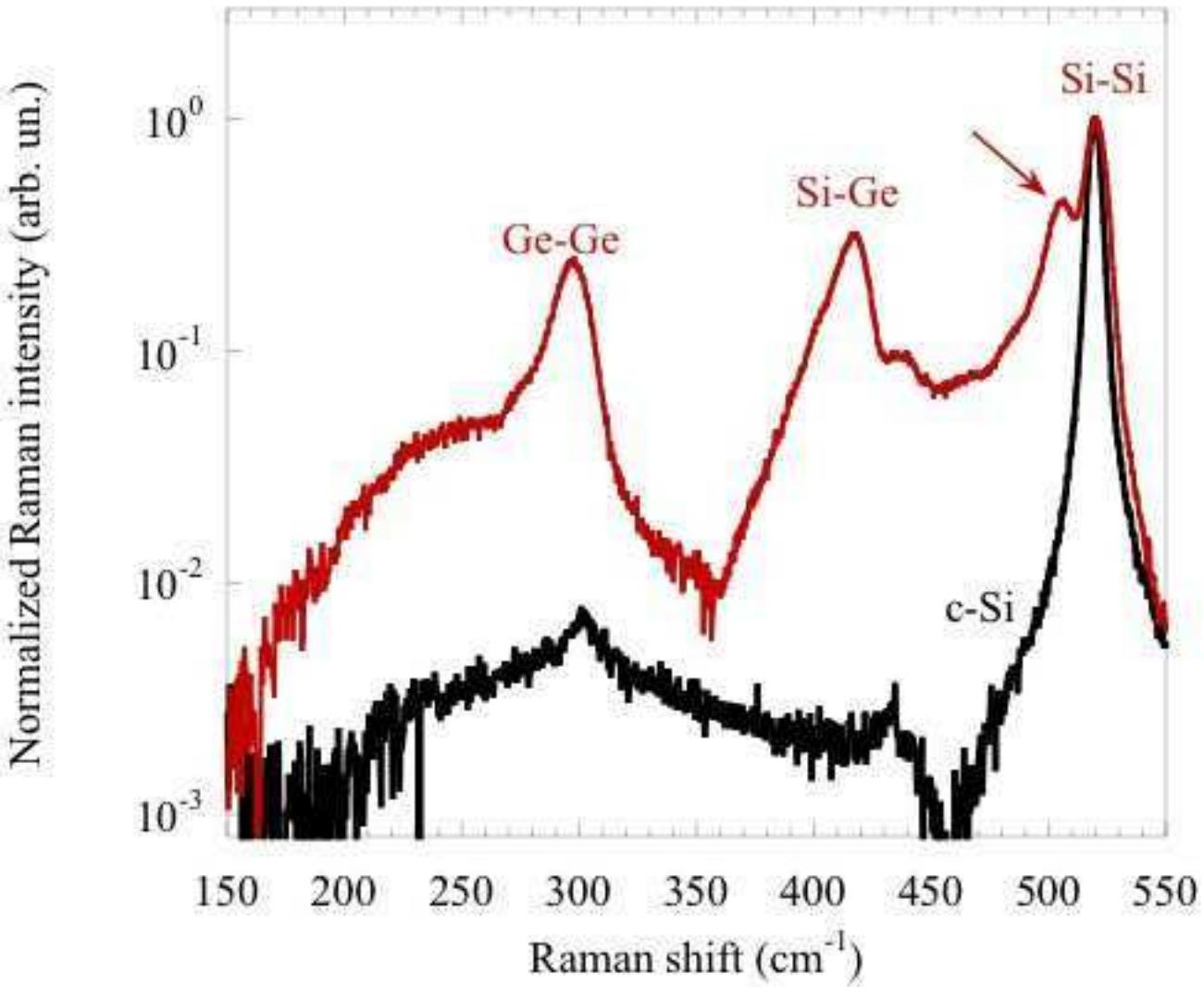

Tsybeskov et al., Fig. 2

Figure

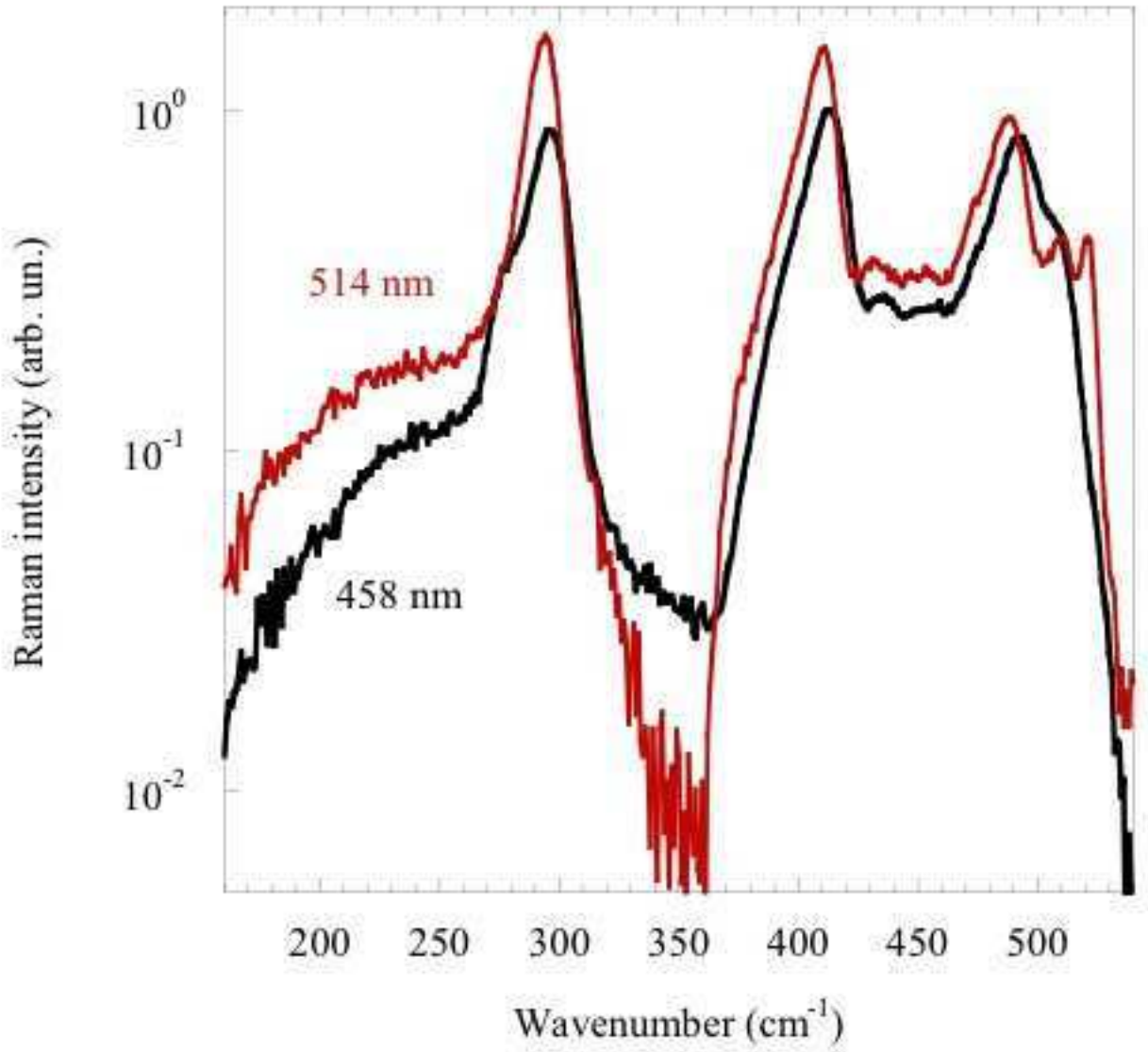

Tsybeskov et al., Fig. 3

Figure

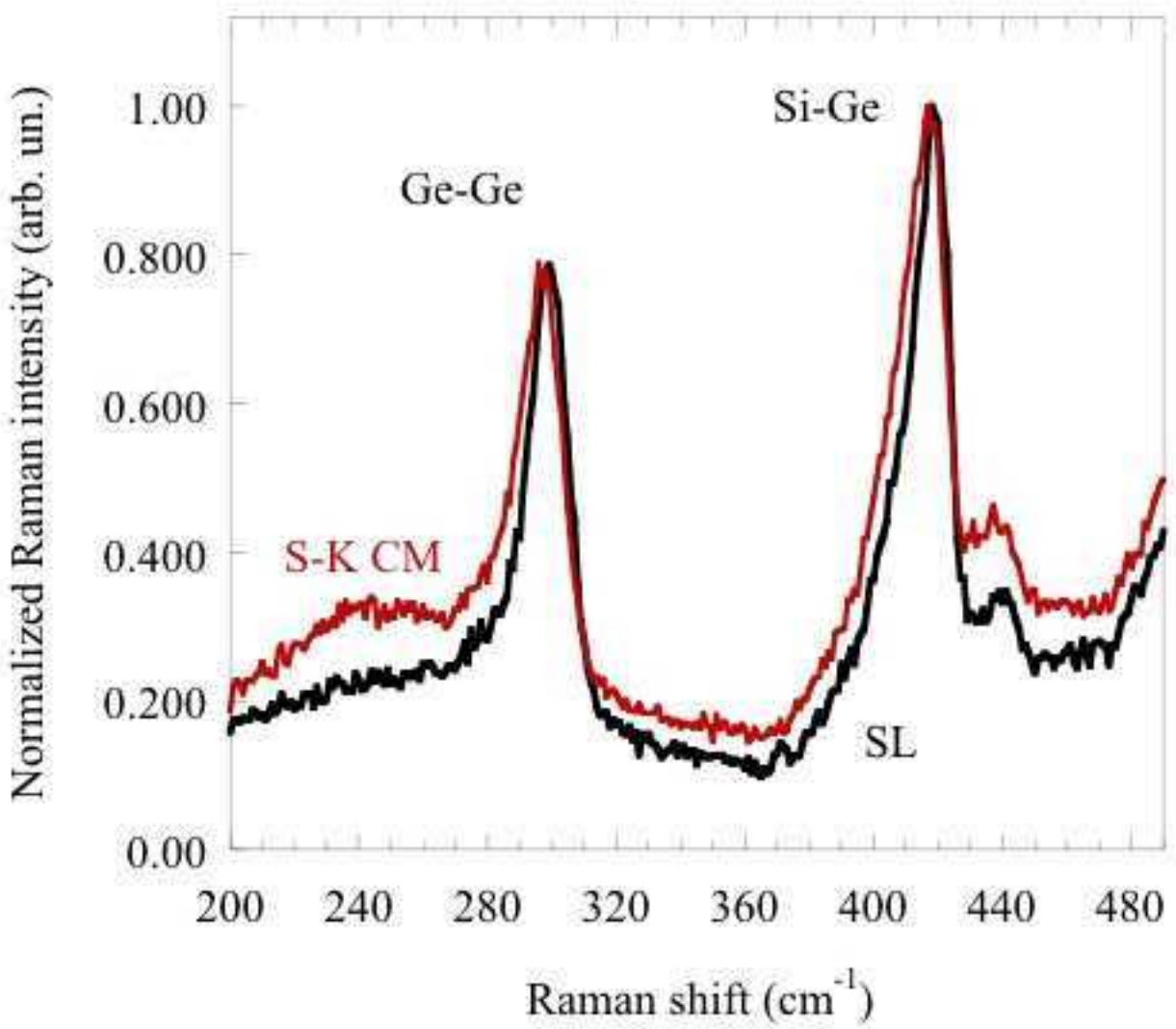

Tsybeskov et al., Fig. 4

Figure

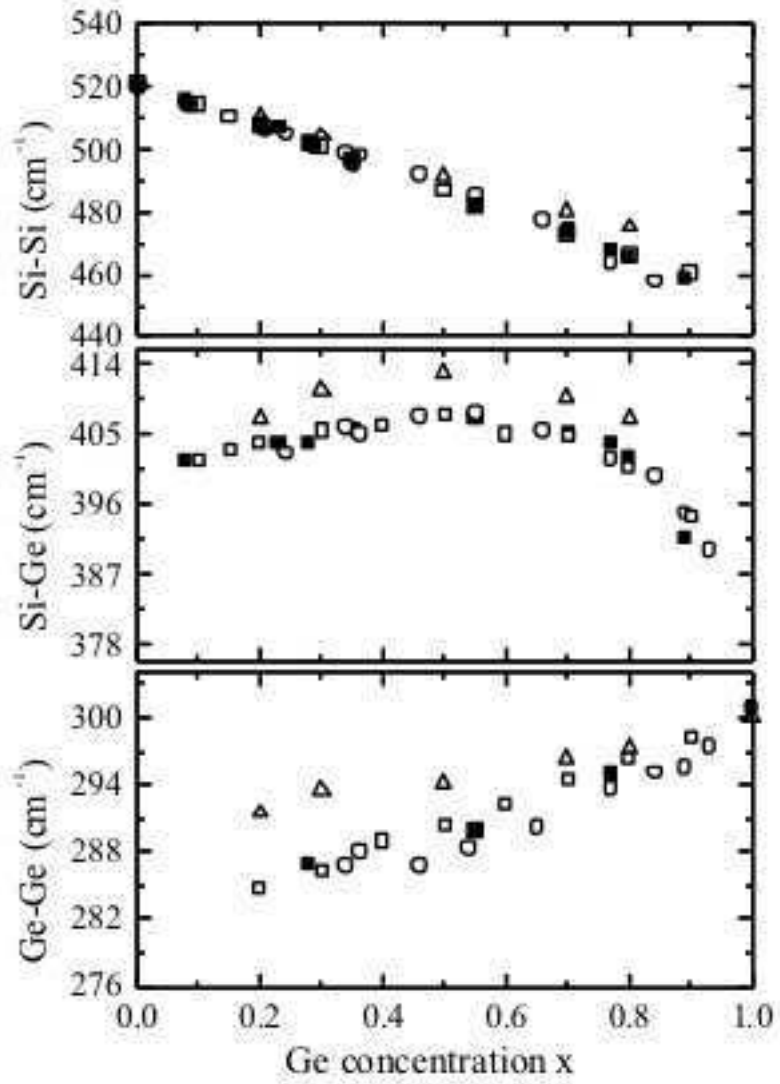

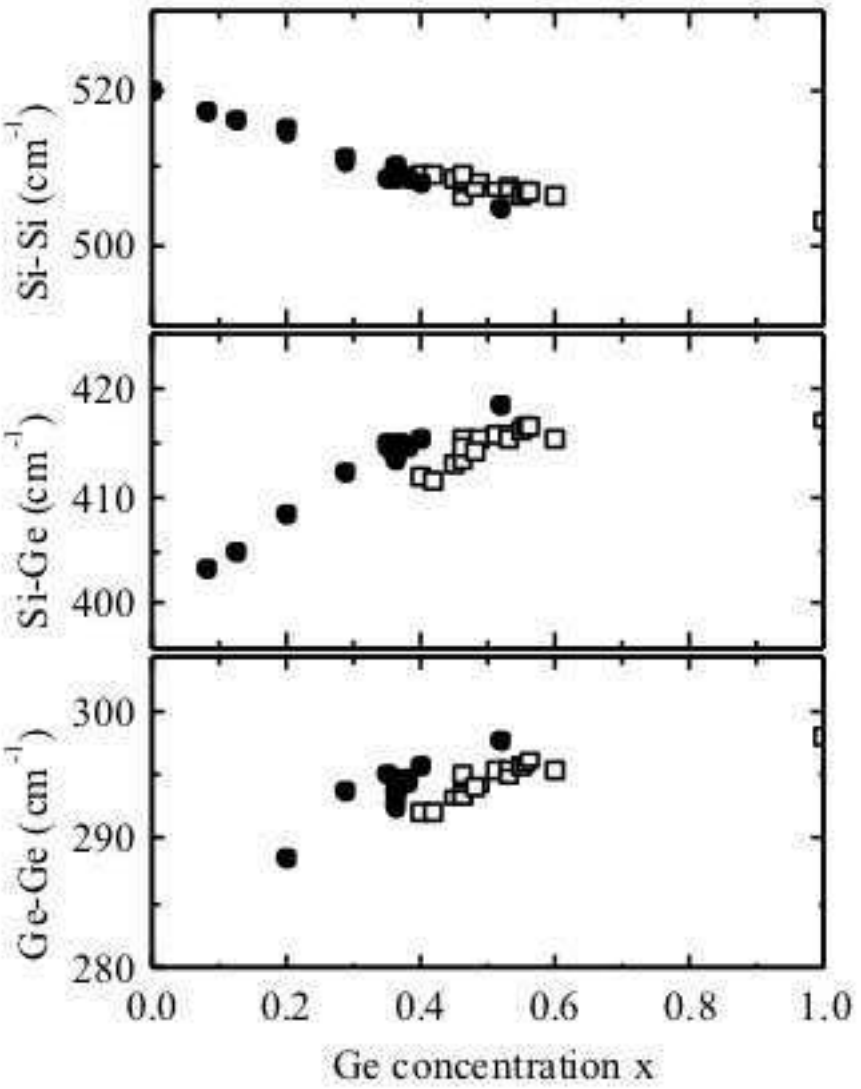

Tsybeskov et al., Fig. 5

Figure

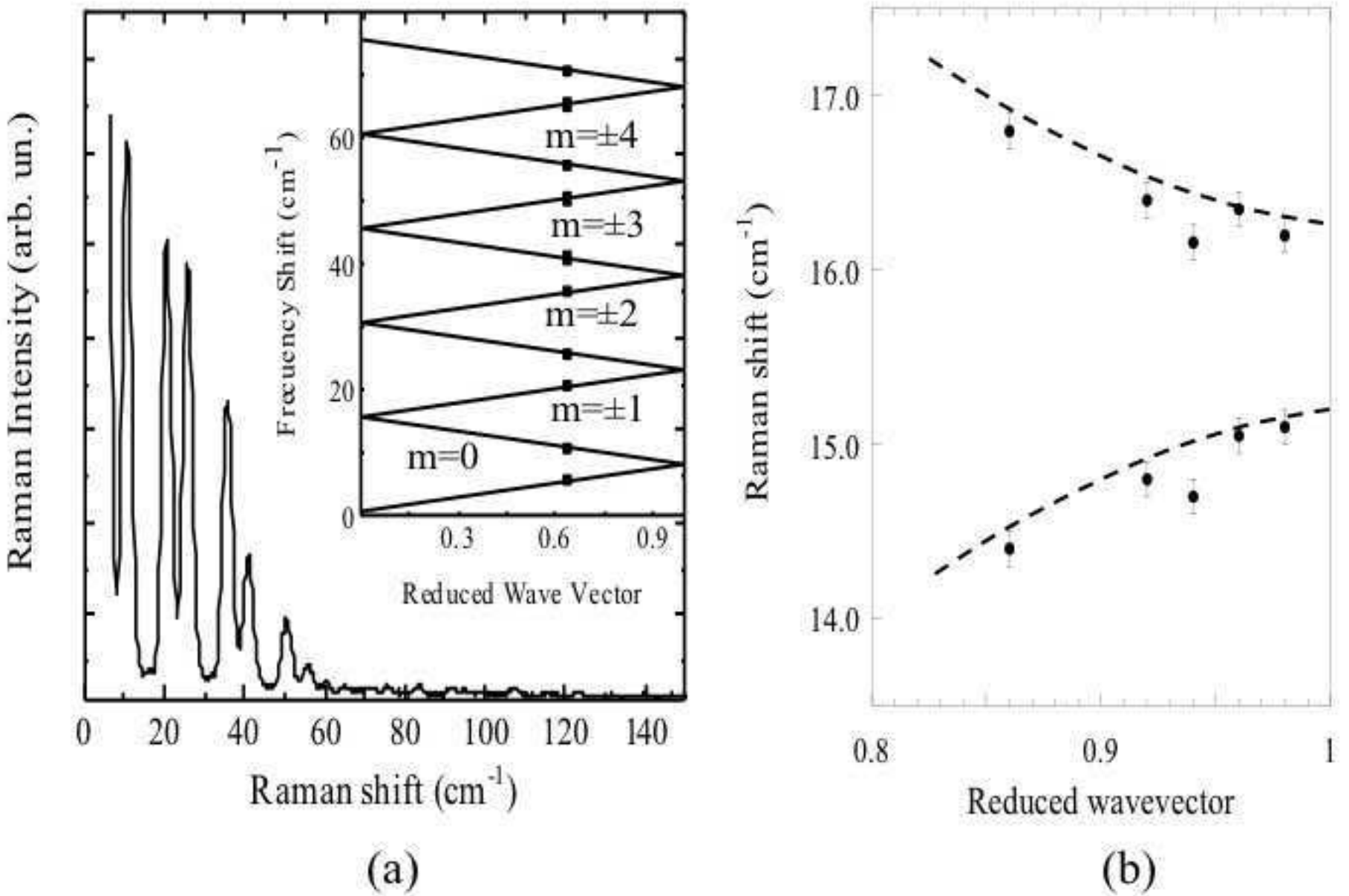

Tsybeskov et al., Fig. 6

Figure

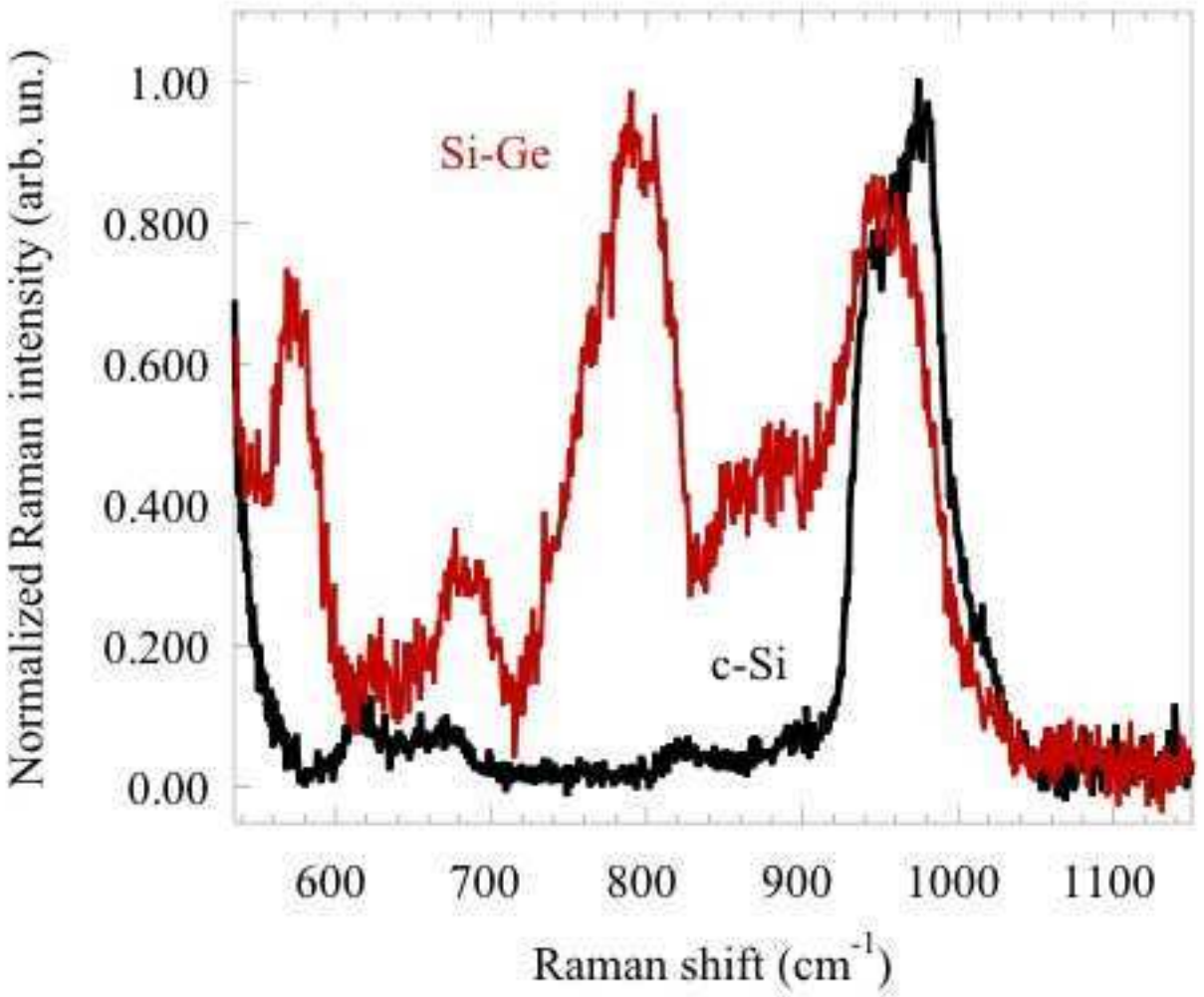

Tsybeskov et al., Fig. 7

Figure

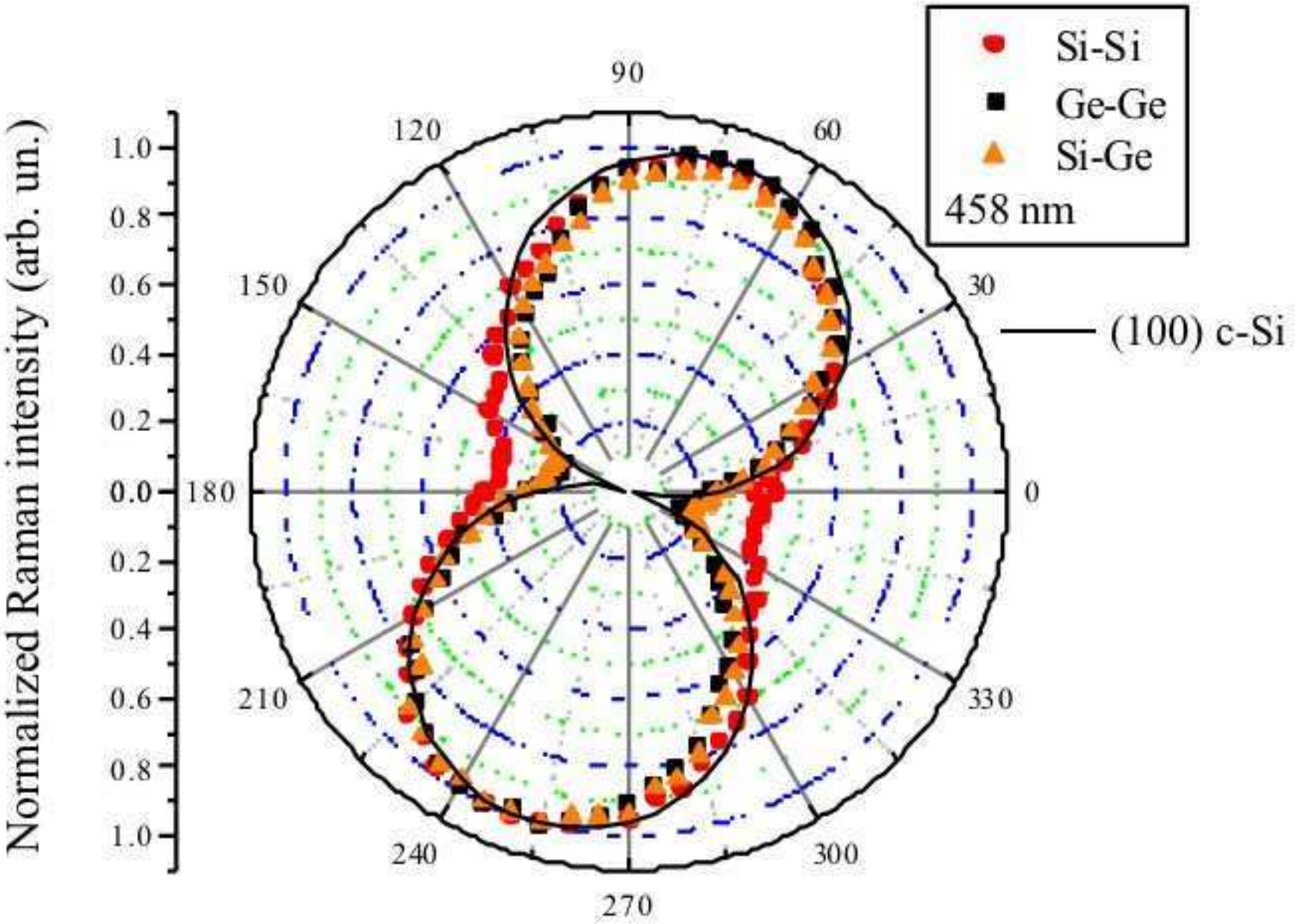

Tsybeskov et al., Fig. 8